Carbon nitride with a tailored electronic structure toward peroxymonosulfate activation: A direct electron transfer mechanism for organic pollutant degradation

Hongbo Ming [a], Xiaoqiong Bian [a,b], Jiajia Cheng [a], Can Yang [a], Yidong Hou [a,*], Kaining Ding [a,b,**], Jinshui Zhang [a,*], Masakazu Anpo [a], Xinchen Wang [a]

[a] *State Key Laboratory of Photocatalysis on Energy and Environment, College of Chemistry, Fuzhou University, Fuzhou 350108, PR China*
[b] *Fujian Provincial Key Laboratory of Electrochemical Energy Storage Materials, College of Chemistry, Fuzhou University, Fuzhou 350108, PR China*

ARTICLE INFO

ABSTRACT

The persulfate-based nonradical reaction process has gained increasing attention in removing organic contaminants, and the process dramatically needs affordable, robust, high-performance heterogeneous catalysts. Herein, dimethyl formamide (DMF) incorporated graphitic carbon nitride (DCN) was synthesized. The molecular engineering of the heptazine unit in DCN improves the electron mobility, strengthens the built-in electric field, and provides abundant active sites, thus enabling DCN to efficiently activate PMS for organic degradation, with 100 % removal of BPA within 12 min. The investigation of the reactive species and electrochemical properties confirmed the direct electron transfer in the PMS activation for organic degradation over DCN. More importantly, DCN can be used as a membrane catalyst in a flowing catalytic unit, enabling continuous water purification and catalyst regeneration. This work provides novel guidance for metal-free catalyst design and profound insights into the persulfate-based heterogeneous catalytic oxidation process for water decontamination technology.

1. Introduction

With the massive discharge of various recalcitrant organic compounds, water contamination is becoming a severe issue affecting water security and sustainability [1–3]. These organic compounds have intrinsically stable molecular structures, potent toxicity, and limited biodegradability, which are immensely arduous to remove through conventional treatment approaches. For instance, as a pollutant widely present in industrial wastewater from plastic manufacturing and electronics industries, bisphenol A (BPA) can mimic the functions of estradiol, disrupt normal endocrine function, and cause adverse human health [4]. Development of efficient and economical water decontamination technologies is thus highly desired. Due to their excellent performance and mild reaction conditions, persulfate-based heterogeneous catalytic oxidation processes have recently gained wide attention in removing organic contaminants [5–9]. There are two typical types of persulfate activation for oxidation processes. One is the radical process that relies on the production of abundant reactive oxygen radicals such

as sulfate radicals ($\bullet SO_4^-$) to initiate oxidations [10–12], and the other is the nonradical pathway (i.e., singlet oxygenation, mediated electron transfer process (ETP) and high-valent metal-induced oxidation) [13–15]. The electron-transfer oxidation mediated by catalysts has received increasing attention owing to its remarkable capacity for efficient degradation of target pollutants through the utilization of minimal persulfate dosages and without the need for external energy input, well addressing the issues suffered from the radical-involved process, including the low steady-state concentration (10^{-12}-10^{-15} M) and short lifetime (10^{-6}–10^{-9} s) of free radicals [16–18]. Application of the ETP pathway in wastewater treatment is now highly dependent on the development of affordable and robust heterogeneous catalysts with high performance toward persulfate activation.

Extensive studies have been conducted on nitrogen-doped (N-doped) carbonaceous materials for persulfate activation toward water decontamination [19–21]. Introduction of electronegative nitrogen atoms relative to carbon atoms (electronegativity: $X_N = 3.04 > X_C = 2.55$) into carbonaceous frameworks can effectively tailor chemical properties of

---

* Corresponding authors.
** Corresponding author at: State Key Laboratory of Photocatalysis on Energy and Environment, College of Chemistry, Fuzhou University, Fuzhou 350108, PR China.
E-mail addresses: ydhou@fzu.edu.cn (Y. Hou), dknfzu@fzu.edu.cn (K. Ding), jinshui.zhang@fzu.edu.cn (J. Zhang).

the surface and electron features of carbons to accelerate electron transfer, endowing N-doped carbons with a unique catalytic behavior toward persulfate activation [22–24]. However, the fabrication of N-doped carbon materials often involves a high-temperature treatment (> 800 °C), which makes the resultant catalysts with a low N content, thus limiting their catalytic performance [25–27]. As a nitrogen-rich polymer, graphitic carbon nitride (CN) consisting of conjugated C and N atoms has been employed as an emerging metal-free catalyst in heterogeneous catalysis due to its facile synthesis, high physiochemical stability, and flexible structural designability [28–30]. Nevertheless, the activity of pristine CN for PMS activation suffers from the relatively chemical inertness and inherently poor electron transportation ability of the C-N conjugated framework. Recently, CN was reported as an excellent support for metal loading because of its stable graphite framework. For instance, Fe single atoms were incorporated into the CN framework, and the formed Fe-N species effectively promoted PMS adsorption and activation [31]. PMS activation process could also be triggered by the electron migration between Co(III)/Co(II) and the high-valent cobalt-oxo species (Co(IV)=O) in the CN framework [32]. Although the reported materials exhibit high PMS activation capabilities, the potential risk of metal leaching remains. Furthermore, transition metals serve as the primary active sites in these materials, while CN does not fully showcase its unique advantages. Therefore, strategies addressing these issues are highly desirable to advance CN toward persulfate-based water decontamination [33–35].

Copolymerization is a well-established synthetic strategy incorporating functional groups into C-N conjugated frameworks [36,37]. Thus, incorporating monomers with electron-rich or -deficient properties can effectively modulate the electronic properties of heptazine units, achieving the controllable adjusting of the sp^2 hybridized π-conjugated structure in the polymeric framework for target-specific catalysis. For example, the precise modulation of local structure in the CN network by incorporating functional groups can optimize the charge distribution and improve the π-electron delocalization, resulting in a built-in electric field in the modified CN framework [38,39]. Therefore, the modified CN could be a good intermediary for electron transfer between PMS and organics, realizing the efficient removal of target pollutants.

To this end, dimethyl formamide (DMF) bearing with acylamino group was selected as the monomer to copolymerize with urea to modify carbon nitride (denoted as DCN) in the present study. With the cyclization of DMF into heptazine frameworks, the formation of a push-pull system induced the delocalization of the π-conjugated electron and improved the electron transport ability, which effectively mediated the electrons migration from the organic to PMS adsorbed on the catalyst. As a result, the as-prepared DCN exhibited an enhanced performance of organic degradation. In addition, the electron transfer mechanism over DCN was investigated by the density functional theory (DFT) calculation and experimental characterizations in detail. Moreover, a flow reaction system was established to investigate the catalytic stability and the practical application of DCN.

2. Experimental

The detailed about chemicals, characterizations, electrochemical measurements, and DFT calculation methods are provided in supporting information.

2.1. Catalyst synthesis

In a typical synthesis, urea (10 g) was ground into a fine powder and mixed with different amounts of DMF (1 mL, 3 mL, 5 mL). Then, the mixture was put into a porcelain boat and was calcined at 550 °C for 3 h with a heating rate of 5 °C min^{-1} in an inert argon atmosphere. The obtained samples were denoted as DCN1, DCN3, and DCN5. Noted that, the yield of DCNx is pretty low when the amount of DMF is increased to 7 mL or higher. CN was prepared via a similar experimental

methodology, with the exclusion of DMF.

2.2. BPA degradation test

In a glass flask reactor, a mixture was prepared by combining 15 mg of catalyst and a 50 mL bisphenol A (BPA) solution with a 20 mg L^{-1} concentration. The initial pH of the BPA solution was 6.3. The temperature of the system was maintained at 25.0 °C using a circulating water bath. After 30 min of stirring in the dark, 40 mg L^{-1} of PMS was introduced into the solution. Throughout the reaction duration, 0.5 mL sample was periodically withdrawn and promptly filtered using a nylon membrane for subsequent analysis. To quench the residual PMS, 0.5 mL of methanol was added to each sample. Control experiments were conducted under identical conditions. The concentration of BPA in the samples was determined using high-performance liquid chromatography (HPLC) equipped with a Waters SunFire C18 column. The HPLC instrument used for this analysis was Agilent Technologies 1260 infinity model. The HPLC column temperature was set at 25 °C. The mobile phase, consisting of methanol and deionized water in a ratio of 70:30 (V$_{methanol}$:V$_{water}$), was pumped through the column at a flow rate of 1 mL/min. Each injection volume was 10 μL. Additionally, the total organic carbon (TOC) content in the BPA solution was determined using a Shimadzu TOC-VCPH analyzer.

2.3. Membrane fabrication and performance evaluation

As-prepared CN and DCN5 samples were made into membranes by a facile process. Briefly, 30 mg powder was uniformly dispersed within 500 mL water and ultrasound for 2 h. The obtained suspension was filtered on polyvinylidene fluoride (PVDF) substrate with a pore size of 0.1 μm under vacuum filtration to get the composite membrane, which was named as CN membrane or DCN membrane. The water permeability, catalytic performance, and regeneration capacity of as-prepared membranes were evaluated through a homemade dead-end filtration system. The aqueous solution containing PMS (40 mg L^{-1}) and BPA (5 mg L^{-1}) was driven through the catalytic membrane using a vacuum pump with a negative pressure of approximately 50 kPa. The water flux of the membranes was calculated as below (Eq. 1).

$$J_0 = \frac{V_P}{A_m \times T} \tag{1}$$

Where J_0 is permeate flux (L m^{-2} h^{-1}), V$_p$ is membrane permeate volume (L), A$_m$ is the effective surface area of membrane (m^2), and T is running time (h). The same procedure was utilized to calculate the flux of the membranes in all experiments. Sampling was done every 0.5 h from the water passing through the catalytic membrane. The catalytic performance of the membrane was evaluated by measuring the removal efficiency of BPA. Moreover, membrane regeneration was achieved by washing the membrane with ethanol and water after the reaction.

3. Results and discussion

3.1. Structure and morphology

Fig. 1a presents the X-ray diffraction (XRD) patterns of DCNx. It is observed that all the samples exhibit prominent diffraction peaks at 13.0° and 27.3°, which originate from (100) and (002) planes of CN, corresponding to the interplanar periodic packing structure and the interlayer stacking of the heptazine framework [40]. With the increase of DMF amount in the starting materials, the peak at 13.0° gradually disappears, and the peak at 27.3° exhibits a reduction in its intensity, suggesting that the addition of DMF changes the conjugated-unit structure in the framework of CN. Fourier transform infrared spectroscopy (FTIR) spectra of the catalysts show the typical characteristic vibrations for CN (Fig. 1b), illustrating that the chemical structure of the
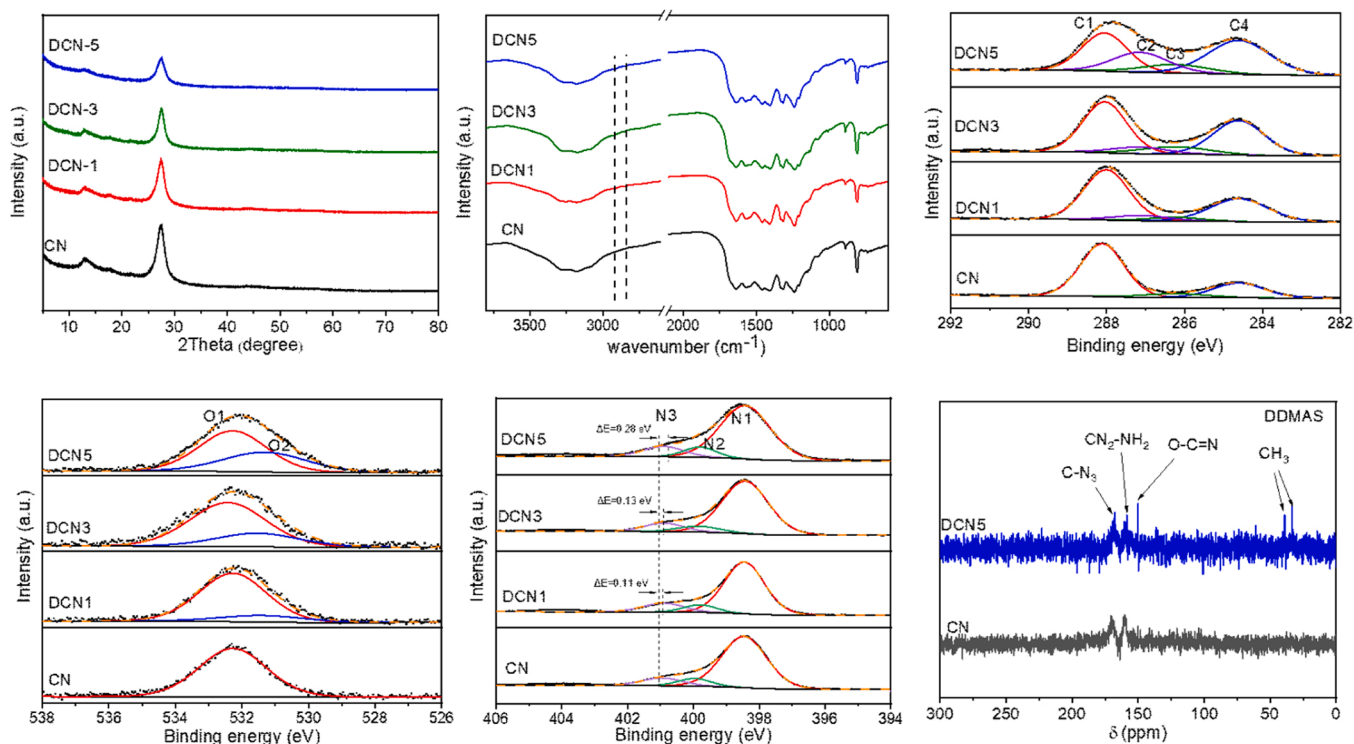
Fig. 1. (a) X-ray diffraction patterns, (b) FTIR spectra, (c-e) C 1s, N 1s and O 1s XPS spectra, and (f) ^{13}C solid-state DDMAS NMR spectra of the samples.

original CN conjugated system is well maintained after incorporating DMF into the CN network. Specifically, the 809 cm^{-1} peak is attributed to the vibration of the s-triazine ring, the vibration bands from 1200 to 1600 cm^{-1} originate from aromatic C-N heterocycles, and the broad bands spanning from 2800 to 3600 cm^{-1} can be ascribed to the N-H and O-H bonds [41]. Moreover, feeble absorption bands at 2921 and 2850 cm^{-1} can be observed in all DCN samples, which are ascribed to the stretching vibration of C–H from –CH$_3$ [38]. These results manifest that the methyl group originating from DMF can be preserved in the thermal-polymerization process.

Scanning electron microscopy (SEM) and transmission electron microscopy (TEM) images were taken to study the morphology and microstructure of the samples. The observation in Fig. S1 displays a typically stacked nanosheet with a porous structure, which agrees with the validated microscopy of CN derived from urea [30]. At relative pressures ranging from 0.8 to 1.0, the N$_2$ adsorption-desorption isotherm displays a characteristic H3-type hysteresis loop, confirming the presence of a mesoporous structure (Fig. S2) [42]. The BET specific surface area of DCN5 (117.7 m^2 g^{-1}) is slightly higher than that of CN (101.8 m^2 g^{-1}). These results illustrate that no noticeable texture changes occur during the incorporation of DMF into the CN framework.

X-ray photoelectron spectroscopy (XPS) surface analyses were measured to infer the possible structure of DCN. The C 1s spectra (Fig. 1c) consist of four peaks at 288.1, 287.1, 286.2, and 284.6 eV, corresponding to sp^2-hybridized carbon (C-N = C), C-O, hydroxyl (C-OH) and C-C/C=C/C-H, respectively [35]. Detailed information on the carbon content of samples (Table S1a) indicates that the C-O bond is successfully incorporated into the framework of DCN, which could be further verified by O1s spectra. As shown in Fig. 1d, all the samples have a peak at 532.3 eV, originating from adsorbed water. However, DCNx exhibits a new peak at 531.1 eV, corresponding to the C-O bond [37]. In the N1s spectra (Fig. 1e), three distinct peaks observed at 398.5, 399.9, and 401.1 eV are assigned to sp^2-hybridized nitrogen (C-N = C), three-coordinated nitrogen (N-(C)$_3$) and terminal amino functional groups (-NH$_2$), respectively.- Notably, the deconvoluted peak at 401.1 eV is gradually shifted to lower binding energy with an increase of

DMF amount in CN, indicating that –NH$_2$ might be replaced by –N–(CH$_3$)$_2$, which exhibits remarkable congruence with the FTIR result. Detailed information on the oxygen and nitrogen content is also listed in Table S1. As shown in Table S1, the amount of C and O atoms increases with the increase of added DMF, but the amount of N atoms decreases correspondingly, which could also be verified by elements analysis (Table S2). According to these results, it is reasonable to infer that the increased C and O atoms originate from –CH$_3$ and C–O, which is derived from DMF incorporated into the CN matrix.

A comprehensive investigation was carried out by measuring the solid-state ^{13}C NMR spectroscopy to validate the modifications during the thermal copolymerization process of urea and DMF. As shown in Fig. S3, CN and DCN5 reveal two prominent resonance peaks at 156.1 and 164.6 ppm, corresponding to C-N3 and CN2-NH2 in tri-s-triazine networks, respectively [43]. Spectral amplitudes of these peaks exhibit a substantial decrement in the DCN5 spectrum, probably due to the fragmentation of planar construction. Besides, the peak in the spectrum of DCN5 presents a shoulder at 151.1 ppm, originating from an increase in the electron density of C atoms owing to the introduction of O atoms with lone pair electrons [36]. Additionally, DCN5 displays three new peaks at 33, 39, and 150 ppm in the solid-state ^{13}C DDMAS NMR spectrum (Fig. 1f), assigned to N-(CH$_3$)$_2$ and O-C=N as described above [38,44]. Based on the characterization results, we proposed the possible polymerization procedure of CN and DCN5 samples (Scheme 1). Generally, urea decomposes to cyanic acid and then assembles into the triazine framework of CN [40]. As soon as the precursor contains DMF, the cyclization of DMF and cyanic acid by dehydration reaction proceeds at high temperatures, then the particular intermediate induces further polymerization to generate DCN.

3.2. Catalytic activity and analysis

The BPA removal over the catalysts is minimal and negligible under the absence of PMS (Fig. S4), which excludes the contribution of adsorption of BPA. The catalytic performance for the BPA degradation was evaluated in different processes. Fig. 2a shows that BPA is hardly
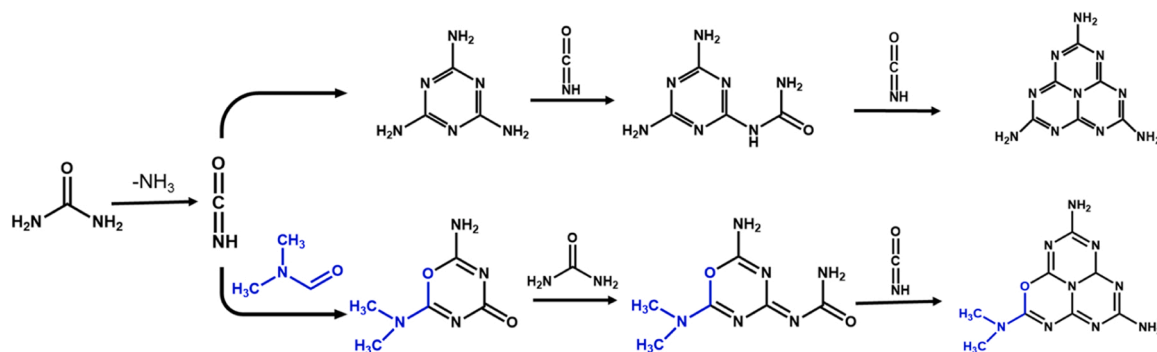
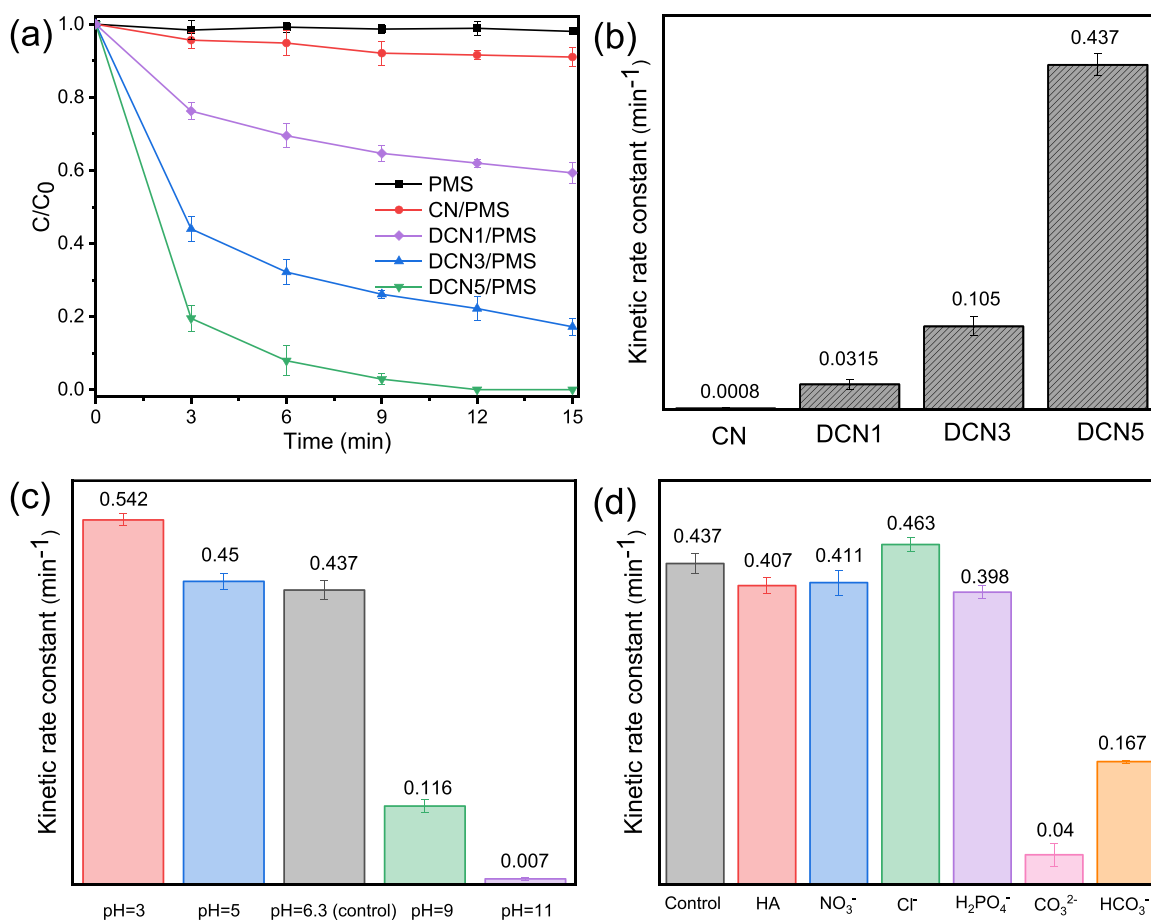**Scheme 1.** Possible grafting procedures of CN and DCN.

Fig. 2. (a) BPA removal rates and (b) corresponding kinetic rate constants for CN, DCN1, DCN3, and DCN5. (c) The kinetic rate constants of BPA degradation under different pH conditions. (b) The kinetic rate constant of BPA degradation in presence of HA, $H_2PO_4^-$, Cl^-, NO_3^- or HCO_3^-. Reaction conditions: [PMS] = 40 mg L^{-1}; [Catalyst] = 0.33 g L^{-1}; [BPA] = 20 mg L^{-1}; [anions] = [HA] = 1.0 mM; T = 25 °C.

removed in the presence of PMS alone, suggesting that PMS does not directly oxide organics at ambient temperature. CN delivers poor performance for PMS activation toward BPA removal. However, all the DCNx samples possess the ability to activate PMS. Specifically, 41 %, 83 %, and 100 % of BPA are removed within 15 min in the DCN1/PMS, DCN3/PMS, and DCN5/PMS systems, respectively. The rate constant was calculated using first-order kinetics to assess the influence of the amount of DMF incorporated into CN on the activation of PMS. Fig. 2b shows that the reaction rate constant significantly enhances with adding more DMF in the precursor for DCNx preparation, and DCN5 demonstrates the best performance of BPA degradation. Furthermore, the 60 % removal rate of the total organic carbon (TOC) is achieved after 60 min

in the DCN5/PMS reaction system (Fig. S5). The catalytic performance comparison between DCN5 and the reported metal-free catalysts was also presented in Table S3. DCN5 has a higher efficiency in BPA degradation with a lower PMS dosage than other catalysts, highlighting the excellent catalytic activity of DCN5.

Fig. 2c displays the effect of the solution pH on the BPA degradation in the DCN5/PMS reaction systems. The BPA removal decreases notably from pH = 3 to pH = 11. The point of zero charges (PZC) for DCN5 is observed at pH = 5.6 (Fig. S6), suggesting that the surface charge of DCN5 is negative in the solution where pH is larger than 5.6. The inhibitory effect on the electrostatic repulsion is strongly associated with the negative charge of the surface of DCN5, which impairs the

adsorption of HSO_5^- and subsequently hampers the activation of PMS, which results in a decrease in the catalytic efficiency for BPA degradation [45].

Common inorganic anions (e.g., Cl^-, $H_2PO_4^-$, and NO_3^-) and natural organic matter such as humic acid (HA) existed in actual wastewater were also considered. As shown in Fig. 2d, adding Cl^-, $H_2PO_4^-$, NO_3^-, or HA scarcely influence BPA degradation. The introduction of CO_3^{2-} and HCO_3^- to the DCN/PMS system impairs the degradation efficacy, primarily due to their alkaline nature in aqueous solution [46]. Furthermore, the catalytic performance of BPA degradation is scarcely changed by altering the water source (Fig. S7). Moreover, by using other pollutants such as phenol, trimethoprim (TMP), 2-chlorophenol (2-CP), ciprofloxacin (CIP), and tetracycline hydrochloride (TCH), the universality of the catalytic performance of DCN5/PMS system toward aqueous contaminant decomposition was assessed. As shown in Fig. S8, the preferable removal of various contaminants in the DCN5/PMS system is also achieved in that degradation system. These results clearly illustrate that DCN5 is an efficient potential catalyst for actual water decontamination.

3.3. Identification of potential radicals

The generation of reactive oxygen species (ROS) was the critical step in PMS activation [7,47]. In order to explore the role of ROS in the catalytic activity of the DCN5/PMS, radical quenching experiments were conducted. As shown in Fig. 3a, the introduction of TBA or MeOH in the reaction system exhibits no apparent effect on the removal of BPA, suggesting that neither •OH nor •SO_4^- is the active species for the removal of BPA [48]. On the other hand, the addition of FFA into the reaction system leads to a noticeable inhibition effect on the degradation

of BPA, suggesting a potential role of $^1O_2$ in the removal of BPA. The validity of FFA quenching $^1O_2$ is still controversial [49]. As shown in Fig. S9, the consumption rate of PMS gradually increases with the increasing content of FFA. Meanwhile, the increase in FFA concentration gradually inhibits the degradation rate of BPA. When the FFA concentration reaches 2.0 mM, BPA degradation in the system is completely inhibited. Therefore, it can be inferred that the presence of FFA in the system competes with BPA for the consumption of PMS. When the FFA concentration is sufficiently high, the PMS would be consumed rapidly, thus suppressing the degradation of BPA. Since the lifetime of $^1O_2$ is about 18 times longer in D_2O than in H_2O [50], the oxidation process could be promoted in the medium of D_2O. However, the solvent replacement of H_2O with D_2O exhibits scarcely change in the catalytic performance of the DCN5/PMS (Fig. 3b). These results exclude the contribution of $^1O_2$ to the removal of BPA in the DCN5/PMS system.

Electron paramagnetic resonance (EPR) technique was used for the investigation of the production of ROS under different reaction conditions, and 5,5-Dimethyl-1-Pyrroline-N-oxide (DMPO) was used as the trapping agent of •O_2^-, •SO_4^- and •OH. $^1O_2$ could be trapped by 2,2,6,6-tetramethylpiperidine (TEMP). As shown in Fig. S10, the signal of DMPO-•O_2^- could not be observed, indicating that •O_2^- is not generated in the DCN5/PMS process. As shown in Fig. 3c, the EPR signals of DMPO-•OH and DMPO-•SO_4^- are barely identifiable in the DCN5/PMS system. Seven apparent signal peaks are observed, which could be attributed to an oxidation product of DMPO (DMPOX) [51]. Meanwhile, Fig. 3d shows the characteristic EPR signal assigned TEMP-$^1O_2$ is detected when DCN5 and PMS are co-present, suggesting that $^1O_2$ is generated in the process of PMS activation. Strangely, the distinct peaks of DMPOX disappear in the presence of BPA, suggesting that BPA is more prone to be directly oxidized by PMS than DMPO. Meanwhile, the EPR
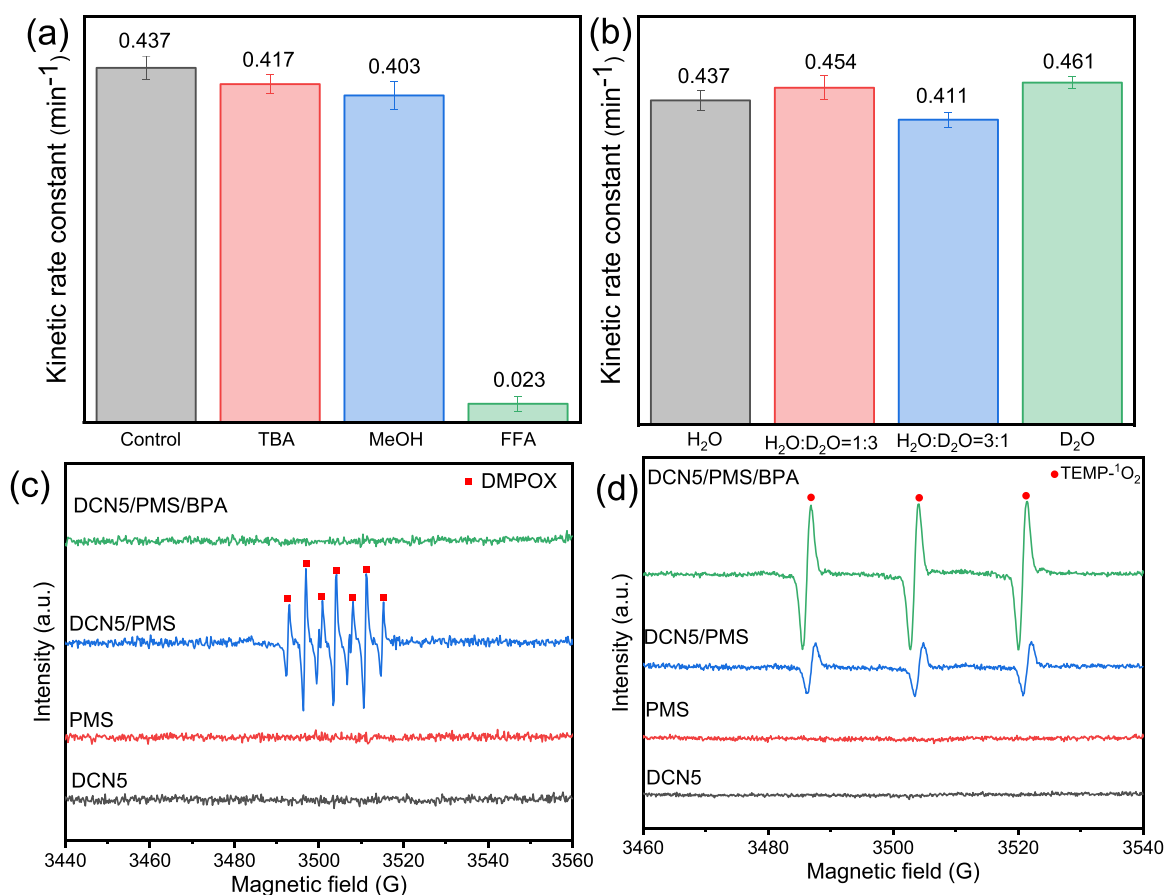

Fig. 3. (a) Kinetic rate constants of BPA degradation in the presence of different scavengers: FFA, MeOH, TBA. (b) The solvent effect on the kinetic rate constant of BPA degradation. (c, d) Spin-trapping EPR spectra in the different reaction systems with DMPO or TEMP as a spin trapping agent.

signal assigned to TEMP-$^1O_2$ increases in intensity after adding BPA into the DCN5/PMS system, suggesting that $^1O_2$ is a product of the decomposition of PMS and is not responsible for the degradation of BPA. These results imply that PMS directly oxidizes organics with DCN as the medium, and radical species are not involved in the degradation reaction.

3.4. Electronic properties and electron transfer between BPA and PMS

The electron paramagnetic resonance (EPR) spectra (Fig. 4a) show a paramagnetic signal with a *g* value of 2.004 for CN and DCN5, which is attributable to unpaired electrons in the CN framework [51]. In comparison to pristine CN, DCN5 shows a significantly strong EPR signal, suggesting the network of DCN5 possesses more free-flowing electrons. Moreover, the electrochemical impedance (ESI) spectra display that DCN5 exhibits an arc with a smaller radius than CN (Fig. 4b), suggesting lower resistance and better electron transport ability of DCN5 than those of CN [52]. The specific features of the electronic structure of CN and DCN were further analyzed by the DFT calculation. The charge distribution in the simulation model structures (Fig. S11) shows different electronic states in CN and DCN. From those results, the electrons over DCN are found to transfer more readily through the push-pull interaction. In addition, the charge distribution on the heptazine unit of CN is depicted in Fig. 4c−d, revealing a symmetrical pattern. Specifically, the electrons in CN are mainly observed around N atoms (red color regions), while holes are observed in the remaining regions (blue color regions). In contrast, the electrons of DCN are mainly localized on the central area of the modulated unit, and the charge accumulation is remarkably intensified. The calculated molecular dipole constant for the representative unit of CN and DCN is 1.69 and 8.65 Debye, respectively. Consequently, a strong built-in electric field can be formed in the DCN

framework [53], which works as an internal driving force to facilitate an efficient electron transfer between organics and PMS adsorbed on DCN. The highest occupied molecular orbital (HOMO) energy was also calculated and shown in Table S4. As shown in Table S4, the HOMO energy of PMS (−7.567 eV) is higher than those of DCN (−6.005 eV) and BPA (−5.504 eV), indicating that the thermodynamically favorable electron transfer of BPA→DCN→PMS results in the oxidation of BPA [54].

The electron transfer between PMS and BPA was experimentally validated through an electrochemistry test. In the test, the electrode was the DCN coated onto a graphite sheet, and an electrocatalytic system was established by placing the BPA and PMS separately in two cells (Fig. 5a) [55]. As shown in Fig. 5b, a weak current is obtained when only DCN exists in each cell. Interestingly, the notable and continuous current is observed when PMS and BPA contact with DCN in separate cells. Moreover, other phenolic organics such as phenol (PE), hydroquinone (HQ), 4-nitrophenol (4-NP), and 4-chlorophenol (4-CP) were also investigated, and their electronic donor abilities were displayed in Fig. S12 [19]. As shown in Fig. S13 and Fig. S14, the organic possessing high electronic donor ability accelerates the electron transfer from organics to PMS, resulting in a high removal ratio.

The linear sweep voltammetry (LSV) analysis (Fig. 5c) was also measured. As shown in Fig. 5c, under applying a negative voltage, the current of the DCN electrode increases with the addition of PMS, implying the presence of a rapid electron transfer from DCN to PMS. The cathodic current of the DCN/PMS system is higher than that of DCN/PMS/BPA, attributable to an electron transfer from BPA to DCN. Meanwhile, the anodic peak is found to shift to lower potential in the presence of BPA, indicating that BPA is easily oxidized. The number of electrons transferred in the PMS for its reduction was also measured by
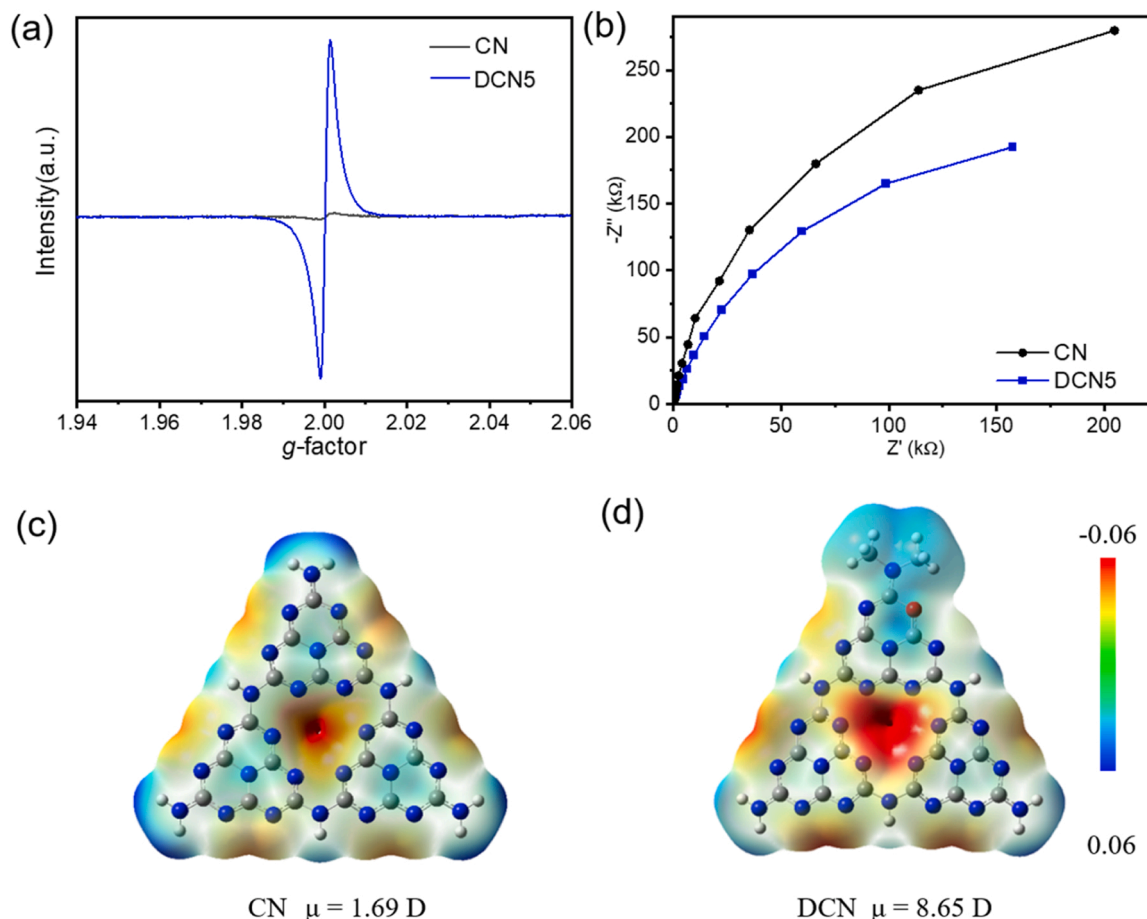

Fig. 4. (a) EPR spectra and (b) EIS Nyquist plots for CN and DCN5. (c-d) Electrostatic potential distribution and molecular dipole of CN and DCN.
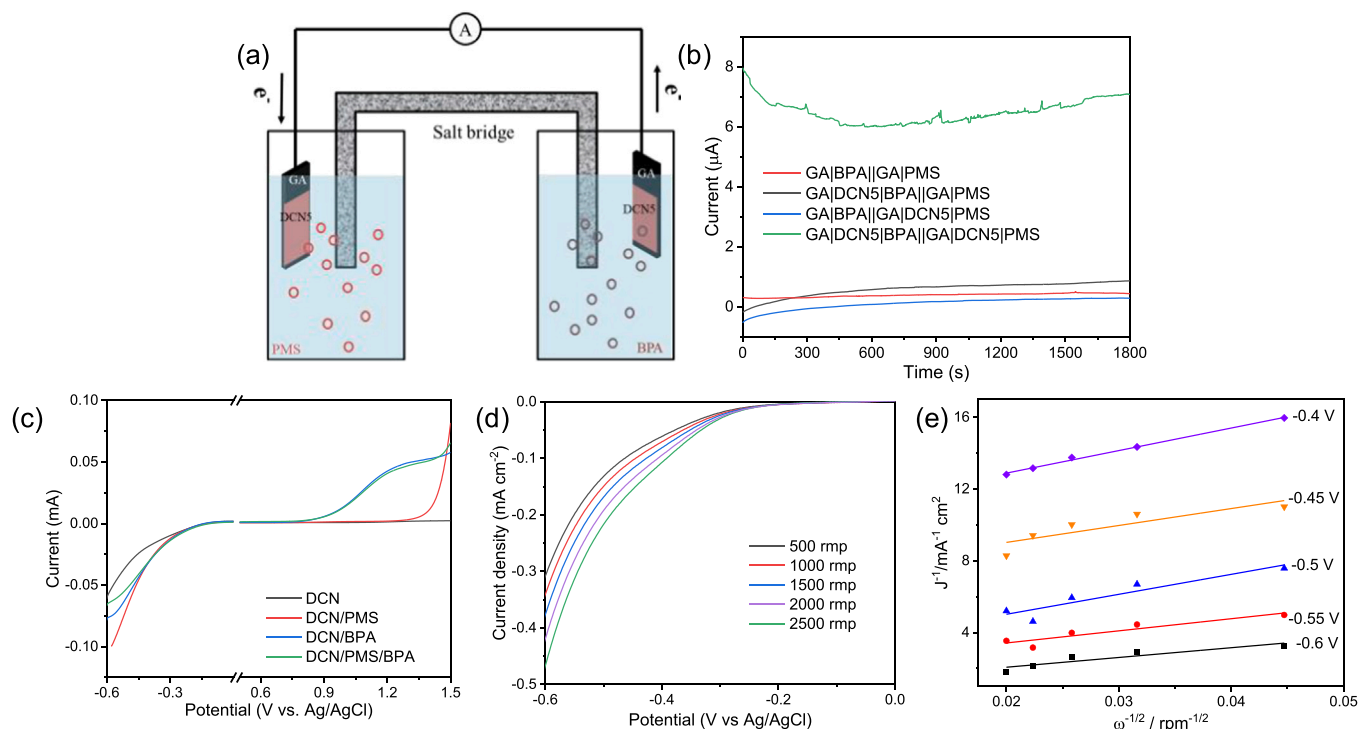
Fig. 5. (a) Scheme for the two-chamber galvanic cell. (b) Current flowing from PMS cell to BPA cell in the various two-chamber galvanic cell systems. (c) LSV curves of DCN5 electrode under different conditions. (d) Rotating disk electrode voltammograms in the DCN5/PMS system and (e) the corresponding Koutecky−Levich plots.

applying the rotating disk electrode (RDE) system. The current is found to increase with an increase in the rotation speed in the LSV (Fig. 5d). On the basis of the K−L plots (Fig. 5e), the number (n) of electrons transferred from DCN to PMS is determined to be 1.27–2.79, suggesting that the activation of PMS on the DCN is a two-electron-dominated route. These results confirm that water purification is achieved through the electron transfer from organics to PMS adsorbed on DCN.

3.5. PMS activation and BPA degradation pathway

More insightful information on the electron transfer process from organics to PMS and the adsorption of PMS on the catalysts was studied by the DFT calculation. Fig. S15 and Fig. S16 show the adsorption behavior of PMS on CN and DCN, and Table S5 displays the adsorption energy and electric charge of PMS and the bond length of O-O in PMS. These results indicate that there is no chemical interaction between CN and PMS. On the other hand, DCN has a distorted spatial structure and delocalized charge density, thus a hydrogen bond could be created when the terminal hydrogen (H) of PMS approaches the nitrogen (N) atom of DCN. Consequently, the optimized adsorption energy of PMS on DCN (−1.35 eV) is higher than that on CN (−0.84 eV), and the O-O bond length of PMS over DCN (1.471 Å) is longer than that over CN (1.464 Å), evidently suggesting that DCN is a better catalyst for the activation of PMS [35]. Moreover, the electric charge of PMS is found to increase from − 1 eV to − 1.054 eV when PMS is adsorbed on DCN, which also confirms the presence of an electron transfer from the catalyst to PMS. As shown in Fig. 6a−b, an increased deformation in the charge density of PMS is observed when it adsorbs onto DCN, suggesting the presence of an efficient electron transfer from DCN to PMS.

Furthermore, the activation pathways of PMS were determined by applying transition state calculations. As shown in Fig. 6c, PMS decomposes into a dissociative SO_4^{2-} and a hydroxyl linked with C atoms of DCN, in good consistent with the experimental result in which PMS was directly reduced to SO_4^{2-} through the two-electron attack. As can be seen in Fig. 6c, compared to CN, DCN exhibits much lower IS and FS energies,

resulting in an easy activation of PMS on DCN. The chemical reaction on the surface was also probed by in-situ Raman spectroscopy. As shown in Fig. S17, when PMS presents on the surface of DCN, two peaks originating from HSO_5^- are observed at around 880 and 1058 cm^{-1}, and a peak assigned to SO_4^{2-} is observed at 979 cm^{-1}, respectively. While, the peaks assigned to HSO_5^- are found to disappear when both PMS and BPA exist on the surface of DCN, indicative of the decomposition of PMS by reacting with organics on DCN [14]. To reveal the degradation pathway, we also tested the composition in the liquid of the reaction system and the eluate of the catalyst after the reaction by using HPLC-MS. Based on the detected products (Fig. S18), we deduced the degradation pathways of BPA in the DCN5/PMS system (Fig. S19), which involves electron transfer, coupling, hydroxylation, alkyl chain scission, hydrogenation, and ring-opening process [56].

3.6. Activity performance and reusability of membrane

The laboratory test of the aqueous contaminant decomposition by the activated PMS is generally conducted by using intermittent sequencing batch reactors, which limits a large-scale water treatment application due to its low efficiency. Even worse, nano-sized catalysts dispersed in wastewater are challenging to collect and are considered potential biological toxicity. Therefore, the development of an efficient and facile continuous water decontamination system is strongly desired. For example, the fabrication of assembly of nano-sized catalysts into the membrane working for pollution removal has been given much attention [24]. Along these lines, DCN5 was fabricated into a membrane, and a dead-end filtration cell was prepared to study the applicability of the membrane in practical application to continuous water decontamination (Fig. 7a–c). For achieving a smooth flow of the mixture of BPA and PMS through a filtration cell equipped with the membrane, negative pressure by a pump was applied. As shown in Fig. 7d, the prepared membrane exhibits weak adsorption of BPA, and the filtration flux rate is higher than 340 L^{-1} m^{-2} h^{-1}. Meanwhile, the DCN membrane exhibits excellent catalytic performance for the degradation of BPA for the first 3 h,
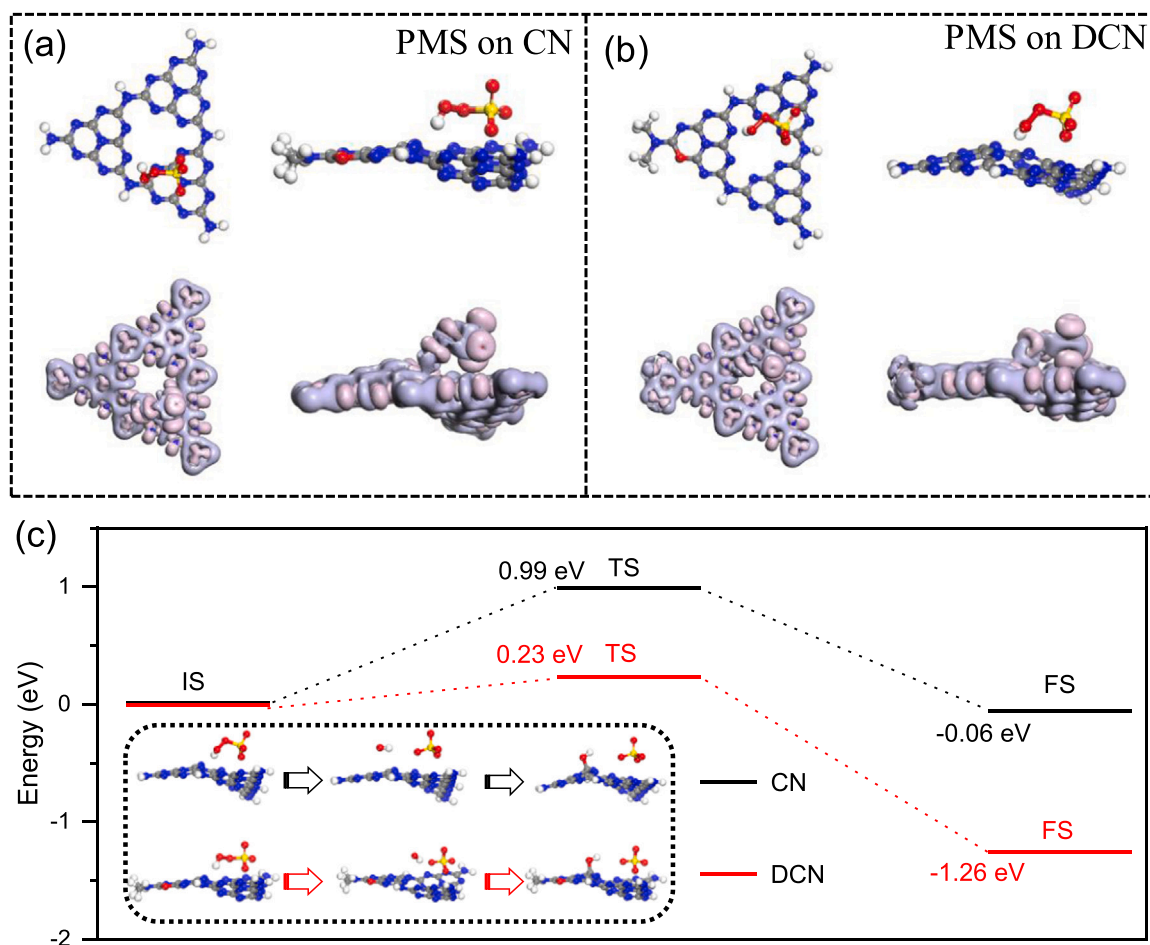
Fig. 6. (a, b) Optimal adsorption configurations and deformation charge densities of PMS adsorbed over CN and DCN. (c) The energy change for PMS activation process over CN and DCN.

and the removal ratio of BPA gradually decreased from 100 % to 54 % in 6 h.

In order to elucidate the underlying cause of the deactivation of catalysts, comprehensive analyses were carried out to study the changes in catalyst structures before and after the reaction. As shown in Fig. S20 and Fig. S21, XRD patterns and FTIR spectra of the DCN membrane before and after the reaction are the same and scarcely change, indicating that the original crystal and chemical structure are well maintained. However, the characteristic peaks of graphitic carbon nitride used in the membrane are relatively weak, being attributed to the accumulation of the intermediate products in the degradation reaction of BPA on the catalyst [57]. According to the XPS spectra (Fig. 8), more C-C/C=C and C-OH groups are found on the used catalyst. Moreover, according to the C 1s and O 1s XPS spectra, it is exhibited that the less C-O bond is incorporated in the DCN framework, suggesting that the intermediate species in the degradation of BPA partially cover the active sites of the DCN catalyst. This situation prevents the activation of PMS and leads to the deactivation of the catalyst. The membrane was cleansed with water/ethanol to remove the adsorbed organic compounds and retested its catalytic activity. The water flux value of the DCN membrane recovers considerably after cleansing, approximately to the initial filtration flux value and the BPA removal ratio in the first cycle (Fig. 7e), demonstrating that the DCN membrane possesses good reproducible performance.

4. Conclusions

We successfully tailored the poly-heptazine unit in carbon nitride by applying a one-step thermal copolymerization of urea and DMF. Introducing an acylamino group into the carbon nitride framework effectively modulated its π-conjugated structure and provided active sites for the adsorption and activation of PMS. The delocalization of π-electrons in DCN also facilitated the electron transfer from the organic molecule to PMS, leading to excellent performance for removing organic compounds. The removal of organic molecules via a particular redox process that occurred on the surface of DCN was successfully substantiated. Specifically, PMS adsorbed on the catalysts, and then the adsorbed PMS was reduced directly to SO_4^{2-} via a two-electron-dominated route without any generation of radicals. Overall, the present work opened a new avenue for designing an electron-transfer medium between PMS and organic molecules by tailoring the electronic structure of a nonmetallic-polymer catalyst, graphitic carbon nitride, which provides a valuable way for developing other persulfate activators.

CRediT authorship contribution statement

Hongbo Ming: Conceptualization, Methodology, Investigation, Writing – original draft. **Xiaoqiong Bian**: Software, Validation. **Jiajia Cheng**: Data curation, Validation. **Can Yang**: Data curation, Resources. **Yidong Hou:** Resources, Conceptualization, Project administration, Supervision, Writing – review & editing. **Kaining Ding:** Software, Supervision, Writing – review & editing. **Jinshui Zhang:** Resources, Writing – review & editing, Supervision. **Masakazu Anpoa:** Supervision, Writing – review & editing. **Xinchen Wang:** Resources, Supervision, Writing – review & editing.
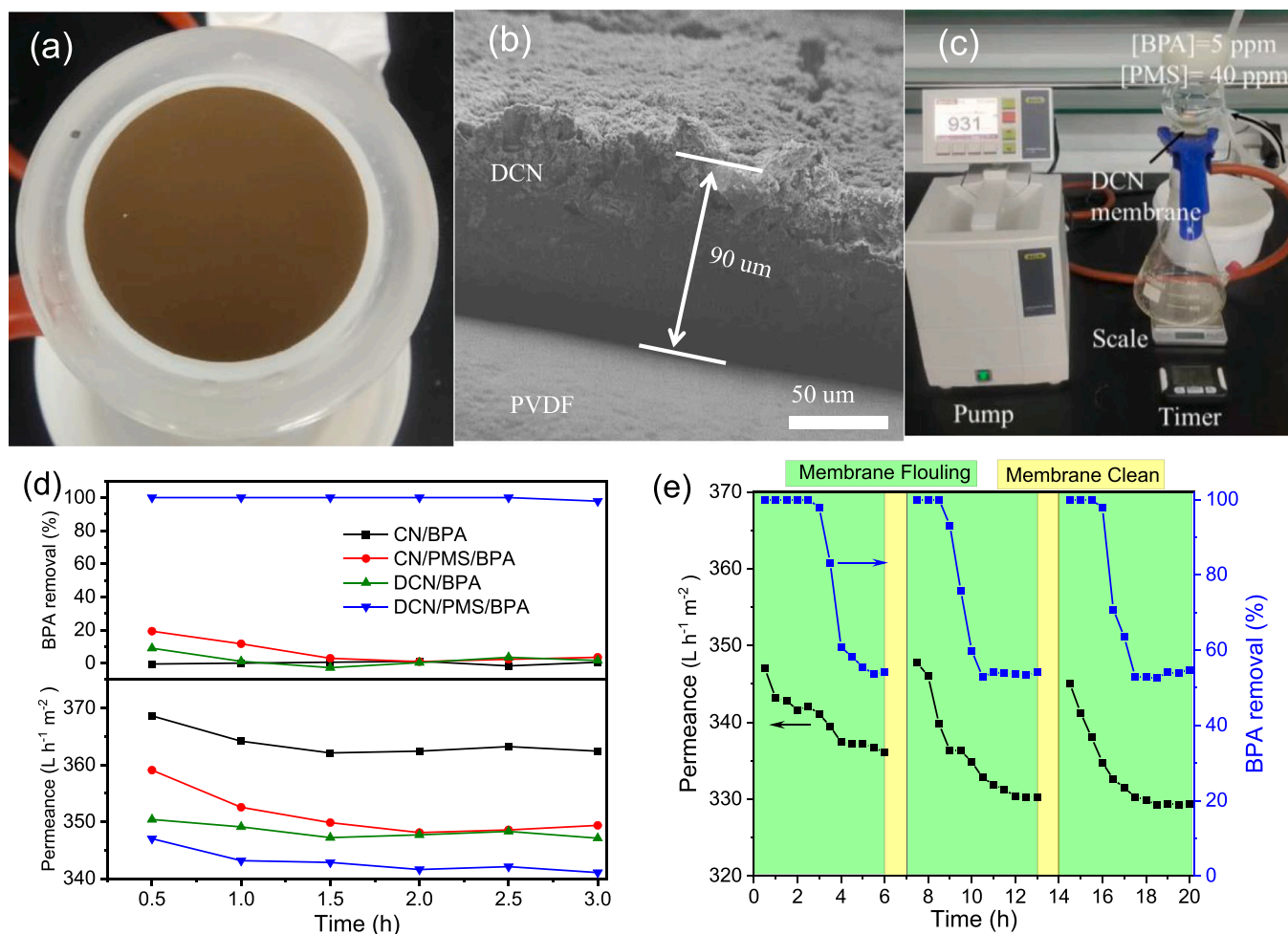
Fig. 7. (a-b) Photograph and SEM of DCN membrane. (c) Photograph of the flow reactor system. (d) BPA removal performance using DCN membrane in different systems; (e) Water permeation flux and BPA degradation using DCN membrane in the multiple tests. Working conditions: $[BPA]_0$ = 5 ppm, $[PMS]_0$ = 40 ppm, T = 25 °C.
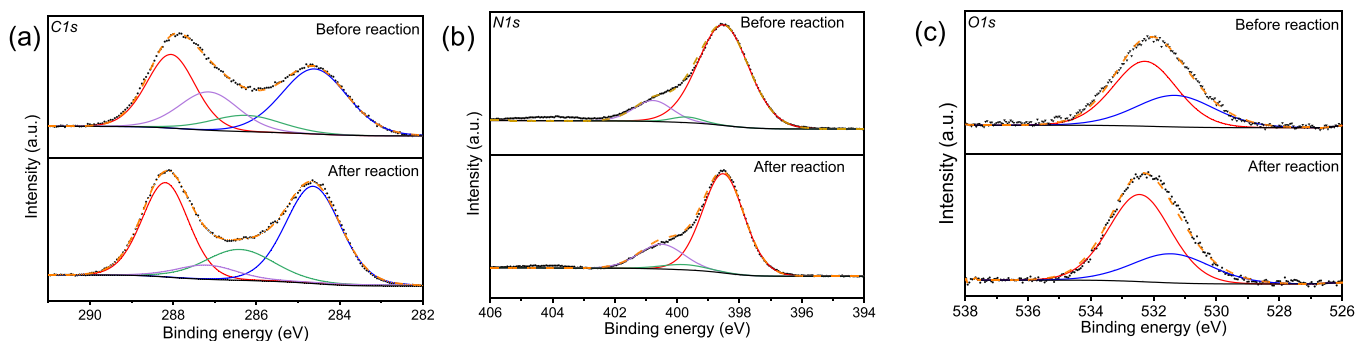

Fig. 8. C 1s, N 1s and O 1s XPS spectra of fresh and used DCN5.

Declaration of Competing Interest

The authors declare that they have no known competing financial interests or personal relationships that could have appeared to influence the work reported in this paper.

Data Availability

Data will be made available on request.

Appendix A. Supporting information

Supplementary data associated with this article can be found in the online version at doi:10.1016/j.apcatb.2023.123314.

References

[1] K. Kümmerer, D.D. Dionysiou, O. Olsson, D. Fatta-Kassinos, A path to clean water, Science 361 (2018) 222–224, https://doi.org/10.1126/science.aau2405.

[2] Z. Cai, A.D. Dwivedi, W.-N. Lee, X. Zhao, W. Liu, M. Sillanpää, D. Zhao, C.-H. Huang, J. Fu, Application of nanotechnologies for removing pharmaceutically active compounds from water: development and future trends, Environ. Sci.: Nano 5 (2018) 27–47, https://doi.org/10.1039/C7EN00644F.

[3] S.D. Richardson, S.Y. Kimura, Water analysis: emerging contaminants and current issues, Anal. Chem. 92 (2020) 473–505, https://doi.org/10.1021/acs.analchem.9b05269.

[4] Y. Ma, H. Liu, J. Wu, L. Yuan, Y. Wang, X. Du, R. Wang, P.W. Marwa, P. Petlulu, X. Chen, H. Zhang, The adverse health effects of bisphenol A and related toxicity mechanisms, Environ. Res. 176 (2019), 108575, https://doi.org/10.1016/j.envres.2019.108575.

[5] J. Lee, U. von Gunten, J.H. Kim, Persulfate-based advanced oxidation: critical assessment of opportunities and roadblocks, Environ. Sci. Technol. 54 (2020) 3064–3081, https://doi.org/10.1021/acs.est.9b07082.

[6] N. Li, R. Li, X. Duan, B. Yan, W. Liu, Z. Cheng, G. Chen, L. Hou, S. Wang, Correlation of active sites to generated reactive species and degradation routes of organics in peroxymonosulfate activation by Co-loaded carbon, Environ. Sci. Technol. 55 (2021) 16163–16174, https://doi.org/10.1021/acs.est.1c06244.

[7] Z.-H. Xie, C.-S. He, H.-Y. Zhou, L.-L. Li, Y. Liu, Y. Du, W. Liu, Y. Mu, B. Lai, Effects of molecular structure on organic contaminants' degradation efficiency and dominant ROS in the advanced oxidation process with multiple ROS, Environ. Sci. Technol. 56 (2022) 8784–8795, https://doi.org/10.1021/acs.est.2c00464.

[8] H. Zhang, C. Xie, L. Chen, J. Duan, F. Li, W. Liu, Different reaction mechanisms of $SO_4\bullet^-$ and $\bullet OH$ with organic compound interpreted at molecular orbital level in Co (II)/peroxymonosulfate catalytic activation system, Water Res. 229 (2023), 119392, https://doi.org/10.1016/j.watres.2022.119392.

[9] M. Huang, Y.S. Li, C.Q. Zhang, C. Cui, Q.Q. Huang, M. Li, Z. Qiang, T. Zhou, X. Wu, H.Q. Yu, Facilely tuning the intrinsic catalytic sites of the spinel oxide for peroxymonosulfate activation: From fundamental investigation to pilot-scale demonstration, Proc. Natl. Acad. Sci. USA 119 (2022), e2202682119, https://doi.org/10.1073/pnas.2202682119.

[10] S. Di, J. Wang, Y. Zhai, P. Chen, T. Ning, C. Shi, H. Yang, Y. Bao, Q. Gao, S. Zhu, Efficient activation of peroxymonosulfate mediated by Co(II)-CeO2 as a novel heterogeneous catalyst for the degradation of refractory organic contaminants: Degradation pathway, mechanism and toxicity assessment, J. Hazard. Mater. 435 (2022), 129013, https://doi.org/10.1016/j.jhazmat.2022.129013.

[11] C. Zhu, S. Zhao, Z. Fan, H. Wu, F. Liu, Z. Chen, A. Li, Confinement of CoP nanoparticles in nitrogen-doped yolk-shell porous carbon polyhedron for ultrafast catalytic oxidation, Adv. Funct. Mater. 30 (2020), 2003947, https://doi.org/10.1002/adfm.202003947.

[12] C. Song, Q. Zhan, F. Liu, C. Wang, H. Li, X. Wang, X. Guo, Y. Cheng, W. Sun, L. Wang, J. Qian, B. Pan, Overturned loading of inert CeO2 to active Co3O4 for unusually improved catalytic activity in fenton-like reactions, Angew. Chem. Int. Ed. 61 (2022), https://doi.org/10.1002/anie.202200406.

[13] Y. Wei, J. Miao, J. Ge, J. Lang, C. Yu, L. Zhang, P.J.J. Alvarez, M. Long, Ultrahigh peroxymonosulfate utilization efficiency over CuO nanosheets via heterogeneous Cu(III) formation and preferential electron transfer during degradation of phenols, Environ. Sci. Technol. 56 (2022) 8984–8992, https://doi.org/10.1021/acs.est.2c01968.

[14] K. Qian, H. Chen, W. Li, Z. Ao, Y. Wu, X. Guan, Single-Atom Fe catalyst outperforms its homogeneous counterpart for activating peroxymonosulfate to achieve effective degradation of organic contaminants, Environ. Sci. Technol. 55 (2021) 7034–7043, https://doi.org/10.1021/acs.est.0c08805.

[15] K.Z. Huang, H. Zhang, Direct electron-transfer-based peroxymonosulfate activation by iron-doped manganese oxide (δ-MnO2) and the development of galvanic oxidation processes (GOPs), Environ. Sci. Technol. 53 (2019) 12610–12620, https://doi.org/10.1021/acs.est.9b03648.

[16] Y.J. Zhang, G.-X. Huang, L.R. Winter, J.J. Chen, L. Tian, S.C. Mei, Z. Zhang, F. Chen, Z.-Y. Guo, R. Ji, Y.-Z. You, W.-W. Li, X.-W. Liu, H.-Q. Yu, M. Elimelech, Simultaneous nanocatalytic surface activation of pollutants and oxidants for highly efficient water decontamination, Nat. Commun. 13 (2022), 3005, https://doi.org/10.1038/s41467-022-30560-9.

[17] J. Dou, Y. Tang, Z. Lu, G. He, J. Xu, Y. He, Neglected but efficient electron utilization driven by biochar-coactivated phenols and peroxydisulfate: polyphenol accumulation rather than mineralization, Environ. Sci. Technol. 57 (2023) 5703–5713, https://doi.org/10.1021/acs.est.3c00022.

[18] J. Miao, W. Geng, P.J.J. Alvarez, M. Long, 2D N-doped porous carbon derived from polydopamine-coated graphitic carbon nitride for efficient nonradical activation of peroxymonosulfate, Environ. Sci. Technol. 54 (2020) 8473–8481, https://doi.org/10.1021/acs.est.0c03207.

[19] W. Ren, L. Xiong, X. Yuan, Z. Yu, H. Zhang, X. Duan, S. Wang, Activation of peroxydisulfate on carbon nanotubes: electron-transfer mechanism, Environ. Sci. Technol. 53 (2019) 14595–14603, https://doi.org/10.1021/acs.est.9b05475.

[20] P. Shao, Y. Jing, X. Duan, H. Lin, L. Yang, W. Ren, F. Deng, B. Li, X. Luo, S. Wang, Revisiting the graphitized nanodiamond-mediated activation of peroxymonosulfate: singlet oxygenation versus electron transfer, Environ. Sci. Technol. 55 (2021) 16078–16087, https://doi.org/10.1021/acs.est.1c02042.

[21] M.R. Azhar, Y. Arafat, Y. Zhong, M. Khiadani, M.O. Tade, S. Wang, Z. Shao, An adsorption–catalysis pathway toward sustainable application of mesoporous carbon nanospheres for efficient environmental remediation, ACS EST Water 1 (2021) 145–156, https://doi.org/10.1021/acsestwater.0c00026.

[22] X. Li, X. Huang, S. Xi, S. Miao, J. Ding, W. Cai, S. Liu, X. Yang, H. Yang, J. Gao, J. Wang, Y. Huang, T. Zhang, B. Liu, Single cobalt atoms anchored on porous N-doped graphene with dual reaction sites for efficient fenton-like catalysis, J. Am. Chem. Soc. 140 (2018) 12469–12475, https://doi.org/10.1021/jacs.8b05992.

[23] Y. Zhang, H. Pan, M. Murugananthan, P. Sun, D.D. Dionysiou, K. Zhang, A. Khan, Y. Zhang, Glucose and melamine derived nitrogen-doped carbonaceous catalyst for nonradical peroxymonosulfate activation, Carbon 156 (2020) 399–409, https://doi.org/10.1016/j.carbon.2019.09.050.

[24] Y. Liu, Q. Lin, Y. Guo, J. Zhao, X. Luo, H. Zhang, G. Li, H. Liang, The nitrogen-doped multi-walled carbon nanotubes modified membrane activated peroxymonosulfate for enhanced degradation of organics and membrane fouling mitigation in natural waters treatment, Water Res. 209 (2022), 117960, https://doi.org/10.1016/j.watres.2021.117960.

[25] X. Duan, Z. Ao, L. Zhou, H. Sun, G. Wang, S. Wang, Occurrence of radical and nonradical pathways from carbocatalysts for aqueous and nonaqueous catalytic oxidation, Appl. Catal. B Environ. 188 (2016) 98–105, https://doi.org/10.1016/j.apcatb.2016.01.059.

[26] X. Chen, W.-D. Oh, T.T. Lim, Graphene- and CNTs-based carbocatalysts in persulfates activation: Material design and catalytic mechanisms, Chem. Eng. J. 354 (2018) 941–976, https://doi.org/10.1016/j.cej.2018.08.049.

[27] H. Yu, L. Shang, T. Bian, R. Shi, G.I.N. Waterhouse, Y. Zhao, C. Zhou, L.Z. Wu, C.H. Tung, T. Zhang, Nitrogen-doped porous carbon nanosheets templated from g-C3N4 as metal-free electrocatalysts for efficient oxygen reduction reaction, Adv. Mater. 28 (2016) 5080–5086, https://doi.org/10.1002/adma.201600398.

[28] Y. Wang, L. Li, Y. Wei, J. Xue, H. Chen, L. Ding, J. Caro, H. Wang, Water transport with ultralow friction through partially exfoliated g-C3N4 nanosheet membranes with self-supporting spacers, Angew. Chem. Int. Ed. 56 (2017) 8974–8980, https://doi.org/10.1002/anie.201701288.

[29] Q. Zhang, Z. Yang, J. Yang, X. Yu, Y. Ling, Y. Zhang, W. Cai, H. Cheng, Carbon nitride simultaneously boosted a PtRu electrocatalyst's stability and electrocatalytic activity toward concentrated methanol, Chem. Commun. 54 (2018) 9282–9285, https://doi.org/10.1039/C8CC03752C.

[30] H. Ming, D. Wei, Y. Yang, B. Chen, C. Yang, J. Zhang, Y. Hou, Photocatalytic activation of peroxymonosulfate by carbon quantum dots functionalized carbon nitride for efficient degradation of bisphenol A under visible-light irradiation, Chem. Eng. J. 424 (2021), 130296, https://doi.org/10.1016/j.cej.2021.130296.

[31] L. Zhang, X. Jiang, Z. Zhong, L. Tian, Q. Sun, Y. Cui, X. Lu, J. Zou, S. Luo, Carbon nitride supported high-loading fe single-atom catalyst for activation of peroxymonosulfate to generate $^1O_2$ with 100 % selectivity, Angew. Chem. Int. Ed. 60 (2021) 21751–21755, https://doi.org/10.1002/anie.202109488.

[32] J. Jiang, Z. Zhao, J. Gao, T. Li, M. Li, D. Zhou, S. Dong, Nitrogen vacancy-modulated peroxymonosulfate nonradical activation for organic contaminant removal via high-valent cobalt-oxo species, Environ. Sci. Technol. 56 (2022) 5611–5619, https://doi.org/10.1021/acs.est.2c01913.

[33] Y. Zhu, Z. Chen, Y. Gao, C. Hu, General synthesis of carbon and oxygen dual-doped graphitic carbon nitride via copolymerization for non-photochemical oxidation of organic pollutant, J. Hazard. Mater. 394 (2020), 122578, https://doi.org/10.1016/j.jhazmat.2020.122578.

[34] M. Wei, L. Gao, J. Li, J. Fang, W. Cai, X. Li, A. Xu, Activation of peroxymonosulfate by graphitic carbon nitride loaded on activated carbon for organic pollutants degradation, J. Hazard. Mater. 316 (2016) 60–68, https://doi.org/10.1016/j.jhazmat.2016.05.031.

[35] Y. Gao, Y. Zhu, L. Lyu, Q. Zeng, X. Xing, C. Hu, Electronic structure modulation of graphitic carbon nitride by oxygen doping for enhanced catalytic degradation of organic pollutants through peroxymonosulfate activation, Environ. Sci. Technol. 52 (2018) 14371–14380, https://doi.org/10.1021/acs.est.8b05246.

[36] X. Zong, L. Niu, W. Jiang, Y. Yu, L. An, D. Qu, X. Wang, Z. Sun, Constructing creatinine-derived moiety as donor block for carbon nitride photocatalyst with extended absorption and spatial charge separation, Appl. Catal. B Environ. 291 (2021), 120099, https://doi.org/10.1016/j.apcatb.2021.120099.

[37] H. Ming, P. Zhang, Y. Yang, Y. Zou, C. Yang, Y. Hou, K. Ding, J. Zhang, X. Wang, Tailored poly-heptazine units in carbon nitride for activating peroxymonosulfate to degrade organic contaminants with visible light, Appl. Catal. B Environ. 311 (2022), 121341, https://doi.org/10.1016/j.apcatb.2022.121341.

[38] C.Q. Xu, W.D. Zhang, K. Deguchi, S. Ohki, T. Shimizu, R. Ma, T. Sasaki, Construction of a push–pull system in g-C3N4 for efficient photocatalytic hydrogen evolution under visible light, J. Mater. Chem. A. 8 (2020) 13299–13310, https://doi.org/10.1039/C9TA13513H.

[39] S. Zhang, Y. Liu, P. Gu, R. Ma, T. Wen, G. Zhao, L. Li, Y. Ai, C. Hu, X. Wang, Enhanced photodegradation of toxic organic pollutants using dual-oxygen-doped porous g-C3N4: Mechanism exploration from both experimental and DFT studies, Appl. Catal. B Environ. 248 (2019) 1–10, https://doi.org/10.1016/j.apcatb.2019.02.008.

[40] J. Zhang, X. Chen, K. Takanabe, K. Maeda, K. Domen, J.D. Epping, X. Fu, M. Antonietti, X. Wang, Synthesis of a Carbon Nitride Structure for Visible-Light Catalysis by Copolymerization, Angew. Chem. Int. Ed. 49 (2010) 441–444, https://doi.org/10.1002/anie.200903886.

[41] H. Fei, J. Shao, H. Li, N. Li, D. Chen, Q. Xu, J. He, J. Lu, Construction of ultra-thin 2D CN-Br0.12/2 %RhOx photo-catalyst with rapid electron and hole separation for efficient bisphenol A degradation, Appl. Catal. B Environ. 299 (2021), 120623, https://doi.org/10.1016/j.apcatb.2021.120623.

[42] G. Zhang, Y. Xu, C. He, P. Zhang, H. Mi, Oxygen-doped crystalline carbon nitride with greatly extended visible-light-responsive range for photocatalytic H2 generation, Appl. Catal. B Environ. 283 (2021), 119636, https://doi.org/10.1016/j.apcatb.2020.119636.

[43] J. Sun, J. Zhang, M. Zhang, M. Antonietti, X. Fu, X. Wang, Bioinspired hollow semiconductor nanospheres as photosynthetic nanoparticles, Nat. Commun. 3 (2012), 1139, https://doi.org/10.1038/ncomms2152.

[44] N. Kamiya, M. Sakurai, Y. Inoue, R. Chujo, Y. Doi, Study of cocrystallization of poly (3-hydroxybutyrate-co-3-hydroxyvalerate) by solid-state high-resolution carbon-13 NMR spectroscopy and differential scanning calorimetry, Macromolecules 24 (1991) 2178–2182, https://doi.org/10.1021/ma00009a006.

[45] L. Xu, L. Qi, Y. Sun, H. Gong, Y. Chen, C. Pei, L. Gan, Mechanistic studies on peroxymonosulfate activation by g-C_3N_4 under visible light for enhanced oxidation of light-inert dimethyl phthalate, Chin. J. Catal. 41 (2020) 322–332, https://doi.org/10.1016/S1872-2067(19)63447-9.

[46] J. Wang, Y. Zhao, C. Li, Z. Yu, Y. Zhang, Y. Li, X. Tan, S. Liu, S. Wang, X. Duan, Peroxymonosulfate oxidation via paralleled nonradical pathways over iron and nitrogen doped porous carbons, Sci. Total Environ. 836 (2022), 155670, https://doi.org/10.1016/j.scitotenv.2022.155670.

[47] C. Liu, L. Liu, X. Tian, Y. Wang, R. Li, Y. Zhang, Z. Song, B. Xu, W. Chu, F. Qi, A. Ikhlaq, Coupling metal–organic frameworks and g-CN to derive Fe@N-doped graphene-like carbon for peroxymonosulfate activation: upgrading framework stability and performance, Appl. Catal. B Environ. 255 (2019), 117763, https://doi.org/10.1016/j.apcatb.2019.117763.

[48] J. Zhang, B. Jing, Z. Tang, Z. Ao, D. Xia, M. Zhu, S. Wang, Experimental and DFT insights into the visible-light driving metal-free C_3N_5 activated persulfate system for efficient water purification, Appl. Catal. B Environ. 289 (2021), 120023, https://doi.org/10.1016/j.apcatb.2021.120023.

[49] Y. Guo, J. Long, J. Huang, G. Yu, Y. Wang, Can the commonly used quenching method really evaluate the role of reactive oxygen species in pollutant abatement during catalytic ozonation? Water Res. 215 (2022), 118275 https://doi.org/10.1016/j.watres.2022.118275.

[50] W.R. Haag, Juerg Hoigne, Singlet oxygen in surface waters. 3. Photochemical formation and steady-state concentrations in various types of waters, Environ. Sci. Technol. 20 (1986) 341–348, https://doi.org/10.1021/es00146a005.

[51] P. Duan, J. Pan, W. Du, Q. Yue, B. Gao, X. Xu, Activation of peroxymonosulfate via mediated electron transfer mechanism on single-atom Fe catalyst for effective organic pollutants removal, Appl. Catal. B Environ. 299 (2021), 120714, https://doi.org/10.1016/j.apcatb.2021.120714.

[52] T. Zeng, S. Jin, S. Li, J. Bao, Z. Jin, D. Wang, F. Dong, H. Zhang, S. Song, Covalent triazine frameworks with defective accumulation sites: exceptionally modulated electronic structure for solar-driven oxidative activation of peroxymonosulfate, Environ. Sci. Technol. 56 (2022) 9474–9485, https://doi.org/10.1021/acs.est.2c00126.

[53] X. Zhang, G. Yang, J. Meng, L. Qin, M. Ren, Y. Pan, Y. Yang, Y. Guo, Acetamide- or Formamide-Assisted In Situ Approach to Carbon-Rich or Nitrogen-Deficient Graphitic Carbon Nitride for Notably Enhanced Visible-Light Photocatalytic Redox Performance, Small 19 (2023) e2208012, doi.org/10.1002/smll.202208012.

[54] X. Zheng, T. Huang, Y. Pan, W. Wang, G. Fang, K. Ding, M. Wu, 3, 3-sulfonyldi-propionitrile: a novel electrolyte additive that can augment the high-voltage performance of $LiNi_{1/3}Co_{1/3}Mn_{1/3}O_2$/graphite batteries, J. Power Sources 319 (2016) 116–123, https://doi.org/10.1016/j.jpowsour.2016.04.053.

[55] E.-T. Yun, J.H. Lee, J. Kim, H.-D. Park, J. Lee, Identifying the nonradical mechanism in the peroxymonosulfate activation process: singlet oxygenation versus mediated electron transfer, Environ. Sci. Technol. 52 (2018) 7032–7042, https://doi.org/10.1021/acs.est.8b00959.

[56] Z.Y. Guo, R. Sun, Z. Huang, X. Han, H. Wang, C. Chen, Y.Q. Liu, X. Zheng, W. Zhang, X. Hong, W.W. Li, Crystallinity engineering for overcoming the activity–stability tradeoff of spinel oxide in Fenton-like catalysis, Proc. Natl. Acad. Sci. USA 120 (2023), e2220608120, https://doi.org/10.1073/pnas.2220608120.

[57] J. Xie, Z. Liao, M. Zhang, L. Ni, J. Qi, C. Wang, X. Sun, L. Wang, S. Wang, J. Li, Sequential ultrafiltration-catalysis membrane for excellent removal of multiple pollutants in water, Environ. Sci. Technol. 55 (2021) 2652–2661, https://doi.org/10.1021/acs.est.0c07418.